# Bayesian analysis and efficient algorithms for single-molecule fluorescence data and step counting

Chiara Mattamira[1], Alyssa Ward[2], Sriram Tiruvadi Krishnan[2], Rajan Lamichhane[2], Francisco N. Barrera[2], and Ioannis Sgouralis[1,*]

[1]Department of Mathematics, University of Tennessee, Knoxville, TN, USA
[2]Department of Biochemistry & Cellular and Molecular Biology, University of Tennessee, Knoxville, TN, USA
[*]Corresponding author: Ioannis Sgouralis, isgoural@utk.edu

**Abstract**

With the growing adoption of single-molecule fluorescence experiments, there is an increasing demand for efficient statistical methodologies and accurate analysis of the acquired measurements. Existing analysis frameworks, such as those that use kinetic models, often rely on strong assumptions on the dynamics of the molecules and fluorophores under study that render them inappropriate for general purpose step-counting applications, especially when the systems of study exhibit uncharacterized dynamics. Here, we propose a novel Bayesian nonparametric framework to analyze single-molecule fluorescence data that is kinetic model independent. For the evaluation of our methods, we develop four MCMC samplers, ranging from elemental to highly sophisticated, and demonstrate that the added complexity is essential for accurate data analysis. We apply our methods to experimental data obtained from TIRF photobleaching assays of the EphA2 receptor tagged with GFP. In addition, we validate our approach with synthetic data mimicking realistic conditions and demonstrate its ability to recover ground truth under high- and low-signal-to-noise data, establishing it as a versatile tool for fluorescence data analysis.

**Keywords:** stepcounting, photobleaching, fluorescence microscopy, data analysis, Markov chain Monte Carlo, statistical learning

## 1 Introduction

The fundamental functions of living cells are carried out or regulated by proteins that assemble in complexes of different sizes [1–3]. Determining the composition of these complexes is crucial for understanding their biological function [4–6]. In recent decades, several fluorescence-based methodologies have been developed to determine protein stoichiometry [7–11], with photobleaching step analysis (PBSA) being one of the most widely used [12, 13]. PBSA relies on the labeling of each molecule of interest with a fluorophore that, during an experiment, initially fluoresces and subsequently photobleaches and stops emitting light within seconds to minutes of the onset of the experiment [14]. Photobleaching events are recorded and used to determine the number of fluorophores within a diffraction-limited fluorescent spot by counting the number of drops in fluorescence intensity over time [15, 16].

The classification of the fluorescence traces obtained from the photobleaching assays is often performed by visual inspection [17–19]. This is time-consuming and, most importantly, subject to human bias. Moreover, single-molecule fluorescence traces are contaminated with noise from multiple sources:

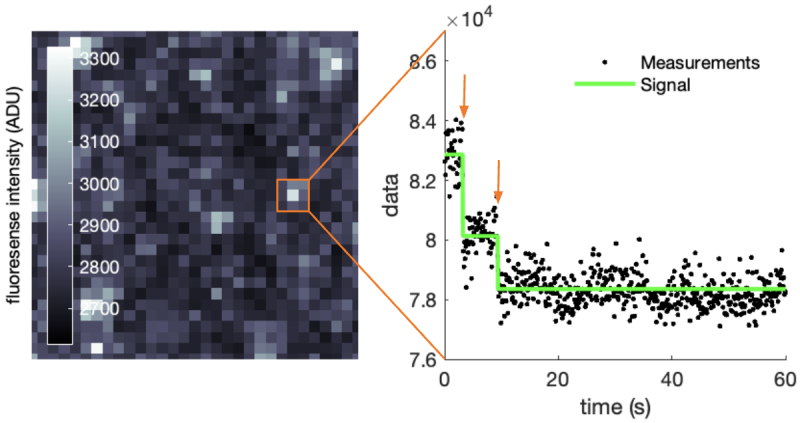


*Figure 1: Photobleaching data and step analysis. The panel on the left shows an example of raw fluorescence data obtained from a TIRF microscopy experiment. Lighter pixels correspond to higher fluorescence levels, which indicate the presence of active fluorophores. For each pixel, we can extract the corresponding fluorescence intensity over time for a set region of interest ($3\mathrm{x}3$ pixels in this case). The extracted time series is shown in black on the right panel. Then our novel Bayesian framework can be applied to determine the MAP signal estimator (green line), provide the total number of steps present, and characterize their time (arrows).*

photon shot noise [20, 21], camera readout noise [22], and optical drift [23]. This results in a large portion of the traces being excluded from visual classification due to their low signal-to-noise ratio (SNR), which leads to additional bias and uncertainty.

Characteristically, the analysis of the data we use in this work, which was acquired using a novel single-molecule pulldown-POP technique (SiMPull-POP) for the TIRF photobleaching assay [19], is currently limited by reliance on user choices, low SRN, and time constraints, among other challenges [24–29]. In this assay, proteins of interest with a fluorescent probe or protein are immobilized within a sample chamber and imaged by total internal reflection fluorescent (TIRF) microscopy. This method provides single-molecule resolution of individual fluorescent intensities over time that can be used to visualize distinct photobleaching events. In turn, this information provides insight into the stoichiometry of protein assemblies, furthering our understanding of how proteins interact and alter cellular behavior.

Several statistical methodologies have been developed to address the challenges and limitations of time series analysis of single molecule data [16, 30–42]. The work on molecular quantification in photoactivation localization microscopy (PALM) [34] using a stochastic approach adapted from aggregated Markov methods provides a prototypical methodology for molecular counting problems. However, its scalability and applicability to very large datasets are limited by the reliance on noise assumptions and computational complexity. Recently, a more comprehensive Bayesian nonparametric method was developed implementing specialized Monte Carlo algorithms [35]. This study serves as a reference for determining both the number of fluorophores and their individual photophysical state trajectories. However, it does present a computational bottleneck when dealing with high molecular counts. Moreover, similarly to other Hidden Markov Model (HMM) frameworks for single-molecule time series analysis [36–38], it relies on the assumption that the system in question evolves in a discrete state space and the state-to-state transitions follow *Markovian dynamics.* Markovianity of measurements is equivalent to exponential duel times [43, 44]. Unfortunately, this is a critical assumption that can be violated, and for this reason various HMM methodologies that employ state aggregates have been proposed [45, 46]. In addition, most often, the transition rates are assumed to be slow compared to the data acquisition

rate, set by the frame rate and exposure period of the cameras used. A Hidden Markov Jump Process (HMJP) approach for fast kinetics was developed to address this limitation [39, 40]. However, despite using weaker assumptions on the data acquisition timescale, HMJP maintains strong kinetic assumptions of the molecules under study. An alternative approach that relaxes the kinetic assumptions is offered by model-independent methods that do not rely on motion models. We can only find one such example in the literature [41] where a generic step detection algorithm is applied and the computations for step identification are carried out. However, this work is limited by the sensitivity to noise levels and step sizes, and computations rely on likelihood ratios with a fixed threshold selection requiring manual user input.

In this study, we develop a new, computationally efficient, model-free Bayesian nonparametric methodology for the analysis of single-molecule fluorescence data and PBSA. Specifically, we provide a novel statistical framework for the analysis of raw PBSA data and propose, for its evaluation, four computational algorithms with increasing complexity. Our first two algorithms are formulated by combining existing Markov Chain Monte Carlo (MCMC) sampling techniques commonly used within the nonparametric Bayesian framework. The third utilizes a novel sampling strategy that aims to address the shortcomings of the first two algorithms and increase the efficiency and reliability of the parameter estimates. Lastly, additional improvements are made through a fourth algorithm, whose performance is largely independent of the MCMC fine-tuning. We also apply our algorithms to experimental datasets obtained using a novel SiMPull-POP technique for TIRF photobleaching assays and validate them using synthetic data with high and low SNR levels. Finally, we compare the quality and efficiency of the four samplers by assessing their ability to recover the ground truth from synthetic data that mimic realistic laboratory conditions.

The remainder of our study is structured as follows. In Results, we demonstrate and validate our algorithms. In Discussion, we describe the general benefits of our sampler and its wider potential for step counting by photobleaching data analysis. Lastly, in Methods, we present our data analysis and acquisition methods, with additional details provided in Supporting Materials.

## 2 Results

We first apply our methods to analyze single-molecule fluorescence data from EphA2-GFP experiments obtained in TIRF photobleaching assays paired with the recently developed SiMPull-POP technique [19, 24, 47]. Next, we validate our methods using data from simulated experiments and demonstrate their ability to accurately recover the ground truth from traces of both high and low signal-to-noise ratios. Lastly, we compare the performance of our most advanced MCMC sampler with that of the three simpler ones described in Methods and demonstrate that its complexity is essential for its high performance.

To facilitate visual comparison of our results with the data under analysis, in the following, we display measurements $w_n$ and signals $U(t)$ after rescaling them as described in appendix C. Our rescaling is essentially a linear transformation that standardizes their units, allowing for a direct scale-free comparison between them without altering their characteristics.

### 2.1 Demonstration with laboratory data

To demonstrate the ability of our methods to analyze experimental data and recover the total number of steps $B$, the background intensity $c_{\mathrm{bck}}$, the intensities of the steps $h_{\mathrm{stp}}^{1:B}$, and the times at which the steps occur $t_{\mathrm{stp}}^{1:B}$, we apply them on raw fluorescence traces [19]. Initially, we choose example data sets with a strong step signature so that they can be easily reproduced with synthetic data when validating the samplers later on. Examples with weaker step signatures are given in the next section, where results

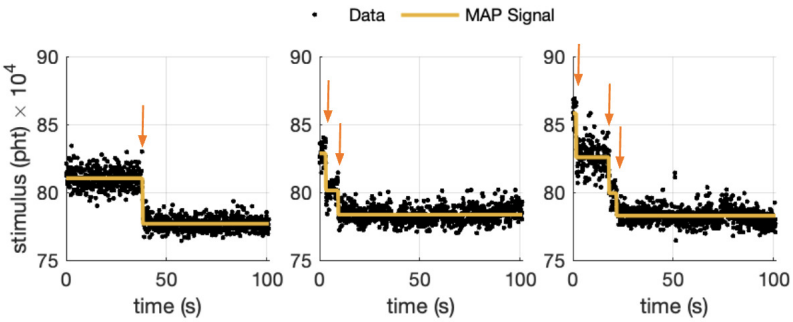


*Figure 2: EphA2-GFP data analysis results for a one-, two-, and three-step traces. Experimental fluorescence reduced data are shown in black, and the MAP signal obtained from applying our most advanced sampler is shown in yellow. Arrows identify the estimated photobleaching events.*

can be compared directly to ground-truth values.

Following common practices, we configure our sampler with the default hyperparameters and run it for $10,000$ iterations. From the generated samples, we discard the first $20\%$ due to MCMC burn-in [48–50]. We then apply the relabeler described in appendix A.1 to ensure the temporal ordering of the steps. The specific values of the hyperparameters used can be found in appendix D. Similarly to all Bayesian approaches, the hyperparameters can potentially affect the outcomes. In order to demonstrate that this is not the situation in our case, we present a comprehensive sensitivity analysis in appendix E.

The results are shown in fig. 2 and fig. 3. Figure 2 shows three characteristic traces with one, two, or three steps along with their corresponding maximum a posteriori (MAP) estimator of the signal, which is the signal with the highest probability according to our model. The number of steps identified by the MAP signal correlates with the stoichiometry of the protein complexes under study [19, 47]. The arrows highlight photobleaching events.

In fig. 3, we show in more detail the experimental data set for the three-step trace, together with the estimated stimulus traces and the signal MAP estimator. We also show a summary of the posterior probability distribution of each variable of interest and the correlation among them. This posterior propagates uncertainty from the measurements, induced by noise and gaps between time points, and provides not only the best choices, but also confidence intervals around our estimators [44, 51].

As we see in fig. 3, our methods detect 3 steps (left panel). In addition, our methods characterize these steps by estimating the intensity $h_{\text{std}}^{1:3}$ and time $t_{\text{std}}^{1:3}$ of each step, and background $c_{\text{bck}}$ (right panel). In particular, the characterization includes estimates of the values and their uncertainly (histograms) as well as correlation between them (scatter plots). As expected, there is a strong negative correlation between some of the intensities of consecutive steps, while no correlation can be detected between the other variables. The observed negative correlation illustrates that our model reproduces a degree of nonidentifiability between the signal of one step and the signal of the preceding step, which is consistent with the additive nature of the signals recorded.

## 2.2 Demonstration with simulated data

### 2.2.1 Sampler validation

To validate the reliability of our analysis, we apply it to synthetically generated time traces that mirror the experimental data used in section 2.1. Hence, we prescribe the total number of steps to 3 which recreates the photobleaching events that take place in the experimental data displayed in fig. 3. In addition, we

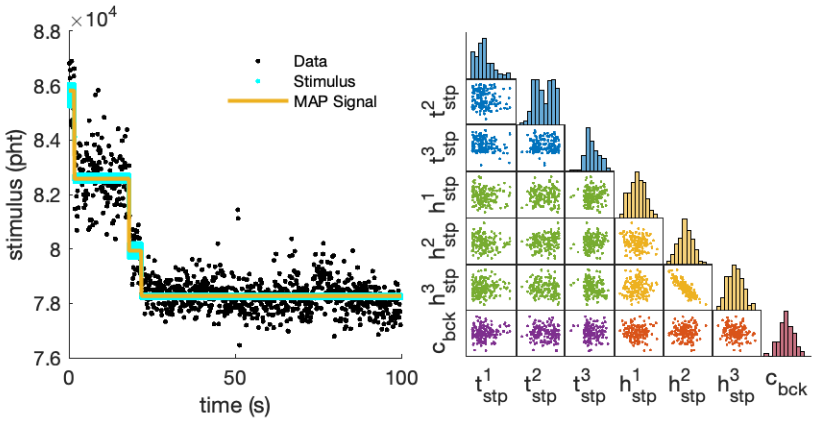


*Figure 3: Laboratory data analysis results. On the left panel, we show the experimental fluorescence reduced data (black) along with the stimuli (cyan) at each measurement time $t_n$ for each sampler iteration after the burn-in period and the MAP signal (yellow) obtained from applying our sampler. On the right panel, we plot histograms of the sampled $t_{\mathrm{stp}}^{1:3}$ (blue), $h_{\mathrm{stp}}^{1:3}$ (yellow), and $c_{\mathrm{bck}}$ (red) after running $10,000$ iterations and discarding the first $2,000$ as well as scatter plots to show the correlation between variables. Thinning was applied to better showcase the density of the plots.*

set the timing and camera parameters according to the settings used to collect the measurements as described in METHODS. Lastly, we prescribe step intensities, times, and background to the MAP estimators obtained from the analysis of the experimental data; that is, we set the ground truth values of our variables to closely match the experimental data set. In this way, we achieve high fidelity between our simulated experiments and those in the laboratory.

The resulting estimates are shown in fig. 4 together with the data, ground truth, and MAP signal (left panel). The close agreement between the ground truth and MAP signal showcases our methods' ability to recover the true values for all quantities of interest. A closer look at how the true value of each individual variable compares with the generated posteriors can also be seen in fig. 4 (right panel). For all estimated variables, the ground truth is close to the highest posterior probability values and, as shown in table 1, the bias is minimal across all variables. This quantitatively indicates that our sampler identifies the ground truth with high accuracy.

To further assess our sampler performance on identifying the correct number of steps along with the correct step characteristics, we consider additional synthetic data sets with low signal-to-noise ratio (SNR) mimicking more demanding experimental conditions. We generate these by reducing all step intensities to $1/5$ of those in the previous example, and maintain all other parameters unchanged. Unlike the higher SNR scenario, which to a certain degree has visually distinguishable steps, the resulting data have a weak signature that is difficult to distinguish from the background. Thus, it cannot be robustly analyzed through visual inspection and instead has to rely on statistical analysis.

Applying our method to this dataset produces the results shown in fig. 5. In this figure, we highlight the estimated times of potential photobleaching events with vertical lines. The density of these lines reflects the certainty of the corresponding photobleaching time. For instance, the first photobleaching event (marked by vertical blue lines) has a strong signature, indicating high certainty in its timing. In contrast, the final step (green lines) has a weaker signature, suggesting greater uncertainty in its timing. To aid in interpretation, we also show histograms of possible photobleaching event times at the top. Here, the spread of a histogram represents uncertainty on the timing, while its integration (i.e., the area

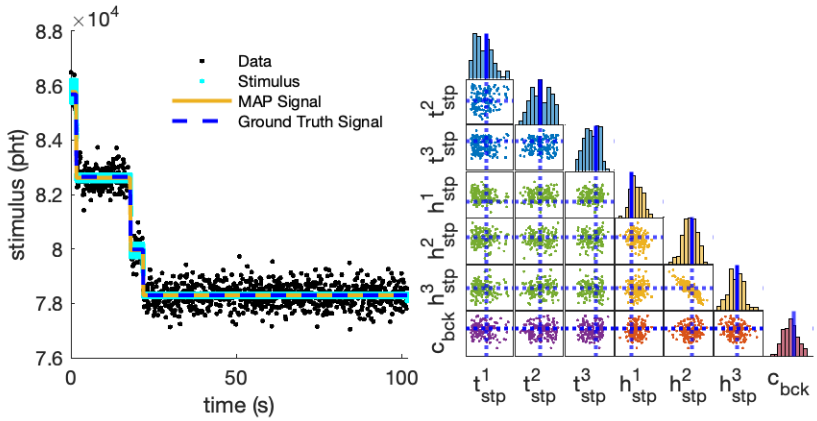


*Figure 4: High SNR synthetic data analysis results. On the left panel, we show the reduced synthetically generated fluorescence data (black) and summary results obtained from applying our sampler. Specifically, the stimulus at each measurement time $t_n$ for each sampler iteration after the burn-in period is shown in cyan, the MAP signal is shown in yellow, and the ground truth signal is shown as a red dash line. On the right panel, we can see a comparison between sampled values for $t_{\rm stp}^{1:3}$, $h_{\rm stp}^{1:3}$ and $c_{\rm bck}$ and true values (blue lines). A total number of $10,000$ iterations was ran and the first $20\%$ were discarded. Thinning was applied to better showcase the density of the scatter plots. A quantitative comparison between sampled and predicted values is shown in table 1.*

under the histogram) indicates the likelihood that the step occurs. Although the estimated stimulus trace shows a higher degree of variation compared to the high SNR scenario, the overall MAP signal still closely follows the true signal. This result demonstrates our methods' ability to accurately recover the ground truth for our target variables, even in cases where the SNR is exceedingly low. A quantitative comparison between the true and predicted values is shown in table 1, where we see that the difference between the mean of the sample and the ground truth remains small.

### 2.2.2 Samplers comparison

Thus far, we demonstrated our method's ability to characterize raw experimental data. For these we applied the fourth sampler described in METHODS which is the most advanced mathematically. In the following, we compare the performance of all samplers by applying each to a synthetically generated data

| Scenario | High SNR | | | Low SNR | | | |
|---|---|---|---|---|---|---|---|
| Parameter | Ground Truth | Sample Mean | Bias | Ground Truth | Sample Mean | Bias | Units |
| $t_{\rm stp}^1$ | $1.69$ | $1.68$ | $-0.01$ | $1.69$ | $1.68$ | $-0.01$ | s |
| $t_{\rm stp}^2$ | $18.12$ | $18.13$ | $0.01$ | $18.12$ | $18.20$ | $0.08$ | s |
| $t_{\rm stp}^3$ | $21.90$ | $21.89$ | $-0.01$ | $21.90$ | $22.11$ | $0.21$ | s |
| $h_{\rm stp}^1$ | $30.30$ | $31.55$ | $1.25$ | $6.06$ | $6.56$ | $0.05$ | pht/ms |
| $h_{\rm stp}^2$ | $26.70$ | $26.50$ | $-0.20$ | $5.34$ | $4.97$ | $-0.37$ | pht/ms |
| $h_{\rm stp}^3$ | $16.80$ | $16.70$ | $-0.10$ | $3.36$ | $3.96$ | $0.60$ | pht/ms |
| $c_{\rm bck}$ | $783.00$ | $782.93$ | $-0.07$ | $783.00$ | $782.96$ | $-0.04$ | pht/ms |

*Table 1: Comparison of ground truth values and mean values of generated samples of $t_{\rm stp}^{1:B}, h_{\rm stp}^{1:B}$, and $c_{\rm bck}$ for both low and high SNR data. Bias is calculated by taking the difference between mean values and ground truth values.*

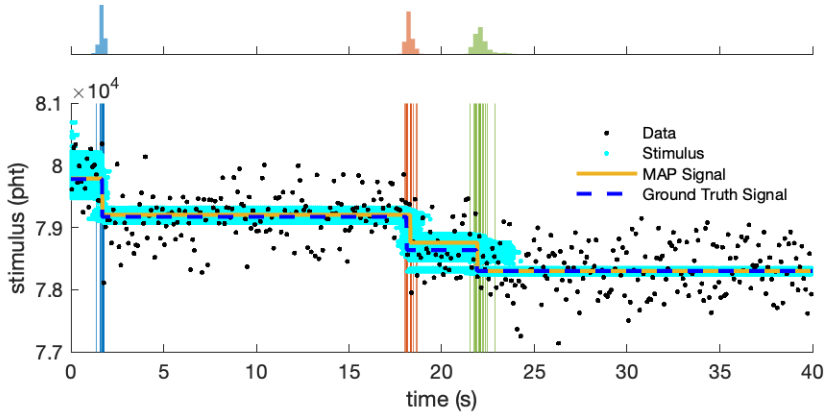


*Figure 5: Low SNR synthetic data analysis results. The bottom panel illustrates the generated data, ground truth signal, MAP signal, and stimuli obtained from our analysis. In the top panel, we plot histograms of the sampled times of the active steps through the experiment run. For clarity, we only plot the first $40$ s of the experiment, which is when all steps occur.*

set and evaluating the degree to which the ground truth is recovered. Moreover, we assess their ergodicity and mixing times. Both are crucial characteristics for reliable data analysis in practical applications.

For consistency, we apply each sampler to the same synthetic data generated in section 2.2.1 that mimic the data used for the experimental demonstration in section 2.1. The results are shown in fig. 6. As showcased by the mismatch between the ground truth and MAP signal, sampler 1 fails to correctly identify the underlying ground truth step locations and intensities. Moreover, both samplers 1 and 2 overestimate the total number of steps, which in turn would lead to incorrect conclusions regarding the stoichiometry of the molecule under study. Notably, both samplers incorrectly place a step towards the end of the collecting time window.

The failure of samplers 1 and 2 to properly characterize our model's posterior is attributed to the nonidentifiability of some of the model parameters, which, in turn, gives rise to multiple local maxima in our probability landscape. For example, different combinations of the background $c_{\mathrm{bck}}$ and the step intensities $h_{\mathrm{stp}}^{1:B}$ can lead to similar stimuli, which paired with non-informative priors result in multiple local maxima in the parameter space. To overcome this challenge, a sampler needs to have good mixing so that it can efficiently explore the entire parameter space without being trapped in the local maxima [48]. Samplers 1 and 2, by updating only one variable at a time, once they reach a local maximum, cannot cross regions of low posterior probability to reach a different high-probability region [48]. Conversely, by making a simultaneous update of multiple parameters, samplers 3 and 4 are able to efficiently explore the parameter space along multiple axes. In particular, performing a stochastic update on one variable and a simultaneous deterministic update on another allows us to direct these samplers towards areas of high probability, as described in more detail in SUPPLEMENT. Samplers 3 and 4 are not only able to identify the correct number of steps, location of the steps, and intensity, but also able to quickly reach the correct solution without getting stuck.

To further assess the mixing properties of each sampler and therefore the overall computational time needed, we obtain the autocorrelation function for the background variable $c_{\mathrm{bck}}$ for each sampler, which we plot in fig. 7. We choose $c_{\mathrm{bck}}$ because this is the only parameter in our model not affected by label switching [44], so our empirical assessment of the autocorrelation function is more robust. The slow initial decay towards zero along with the overall pattern of the autocorrelation functions of samplers 1 and

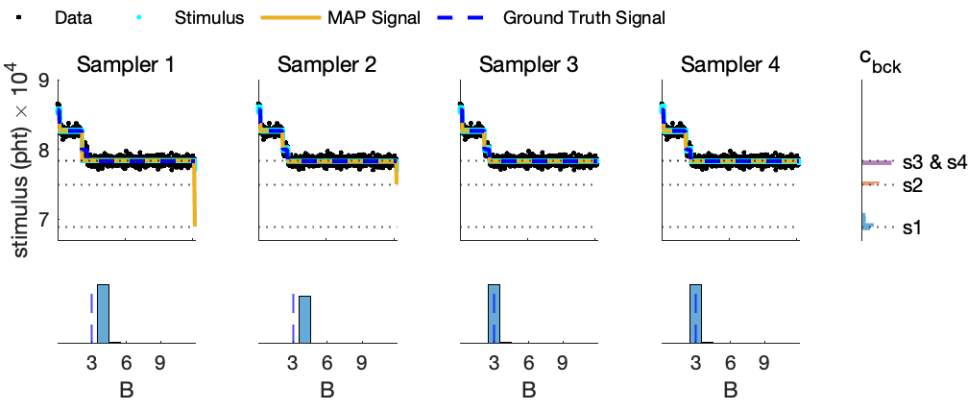


*Figure 6: Samplers comparison with synthetic data. The first four panels display the generated data, stimuli, MAP and ground truth signal for each sampler. Underneath each one, we plot histograms for their respective total number of active steps. The top right panel shows histograms for the background samples $c_{\mathrm{bck}}$ for each sampler (s1-s4).*

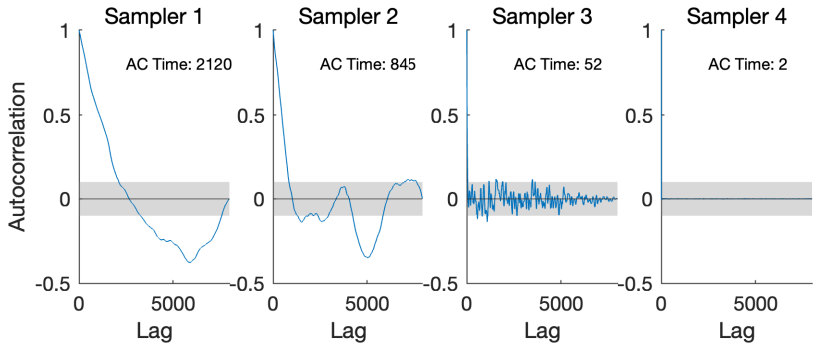


*Figure 7: Plots of the autocorrelation function (ACF) of the background parameter $c_{\mathrm{bck}}$ sampled from each of the four samplers. Autocorrelation times are displayed in the top right corner of each plot. The number of lags used corresponds to the number of samples kept after the burn-in period.*

2 indicate a significant degree of correlation between samples. However, the autocorrelation functions of the more advanced samplers present a fast initial decay and settle around zero thereafter, indicating that there is little to no relationship between the samples. This means that the overall computational time required to generate a sufficiently large number of samples is significantly lower for samplers 3 and 4, speeding up the analysis and allowing more traces to be analyzed. We also calculate the autocorrelation time, which we define as the first lag where the absolute value of the autocorrelation function falls below 0.1 and therefore indicates how quickly the samples become decorrelated. The autocorrelation times of samplers 1, 2, 3, and 4 are 2120, 845, 52, and 2 lags, respectively. This highlights sampler's 4 high efficiency and rapid mixing that renders it the sampler of choice for general applications, especially those involving high-throughput data analysis.

## 3 Discussion

Analysis of single-molecule fluorescence traces with an efficient statistical framework is an essential requirement to determine the biological functions and dynamics of molecular clusters within diffraction-

limited regions [19, 24, 29, 47]. Following a photobleaching experiment, this task reduces to accurately and quickly determining the number of steps present in the acquired fluorescence time series. This allows investigators to deduce the stoichiometry of the molecules under study and gain insight into their structural and functional functions. The work we present here provides a novel statistical model to represent fluorescence traces and four different algorithmic procedures to analyze them. Our methods not only determine the total number of steps, but also provide full posterior distributions for individual steps and their characteristics. We do so without relying on restrictive assumptions on the dynamics of the molecules under study, providing instead a kinetics-independent approach that can be extended to a variety of single-molecule fluorescence experiments.

Our methods were illustrated by applying them to raw data from TIRF microscopy experiments. We demonstrated our method's ability to recover the number of steps present and validated our method by reproducing the experimental settings using synthetically generated data. We showed that our method is able to accurately recover ground truth in both low- and high-SNR scenarios. Moreover, we evaluated the quality of our methods by evaluating their mixing properties and found that our sampler is able to efficiently explore the parameter space, converges rapidly, and has low autocorrelation.

The contribution that this work brings will particularly apply to data sets that are effected by higher degrees of noise and have a weaker signature, allowing practitioners to tackle experiments that have been inaccessible before. Data acquired at the single-molecule level, such as the SiMPull-POP data explored here, are often accompanied by a high background and noise, which can obscure and convolute the data analysis process. By applying a fully automated statistical approach that is independent of user's surjective input, as we have shown here, it can both confirm and compare current data quantification methods to validate experimental data results. In addition, it will help reduce potential data quantification bias, reveal photobleaching steps that are difficult to distinguish by visual inspection, and provide a more detailed characterization of the data at hand.

Although in this study we applied our sampler to a specific experimental data set, the methodology we propose can be generalized and applied more broadly within the sphere of photobleaching step analysis. However, despite its novelty and computational efficiency, our method presents certain limitations. First, it is mathematically demanding, so its adoption is based on existing software. We provide a prototype implementation (source code and graphical user interface) in Supporting Materials and in our GitHub repository [52]. Second, our method is sensitive to experimental details related to data acquisition hardware. Currently, our implementation supports fluorescence data from one-channel recordings acquired via wide-field microscopes equipped with either EMCCD or CMOS cameras. Nevertheless, two-color imaging, FRET, or even rapid single-photon recordings can be incorporated, but only with nontrivial modifications to our detection setup. Obviously, such cases require problem-specific implementations that will be the focus of future studies.

# 4 Methods

## 4.1 Data analysis

We develop a specialized statistical model for data analysis that includes physically faithful signal, stimulus, and noise representations. The model that we formulate does not use kinetic schemes or other dynamical representations, so it can be applied in situations where the dynamics probed may or may not be Markovian. We apply Bayesian principles to provide parameter estimates and provide specialized computational procedures in order to evaluate the values of our estimators. That is, we develop four different MCMC samplers with increasing sophistication. For details, see formulations in Supplement. Specifically, refer to appendices A.1 and A.3 for our model formulation, and appendices A.5 and B for

our computational approaches.

### 4.2 Data acquisition

For the demonstrations shown in RESULTS, we used synthetic and real-life data from single-molecule experiments.

The *laboratory data* are obtained by the SiMPull-POP TIRF photobleaching assay, as detailed in [19] of a full-length EphA2 fused to the C-terminal GFP that was stably expressed in mammalian cells DU145 (ATCC® HTB-81).

The *synthetic data* is obtained by simulating the model of appendix A.1 using standard pseudorandom operations. For the simulations, we set the timing and camera parameters according to laboratory settings (see above) and generated measurements of equal size spanning an equivalent period of real time. We list our specific values in appendix D. For all simulations, we prescribe the values of $c_{\mathrm{bck}}$, $B$, $\bar{h}_{\mathrm{stp}}^{1:B}$, and $\bar{t}_{\mathrm{stp}}^{1:B}$. The ground truth values are maintained for comparison with MCMC, but otherwise not used.

## Author contributions

C.M. contributed to the analysis methods, computational implementation and software development. C.M. and I.S. prepared the manuscript. A.W., S.T.K., R.L., and F.N.B. provided the experimental data and commented on the manuscript. I.S. conceived the research and supervised all aspects of the project.

## Conflict of interest

The authors declare no conflict of interest.

## References


[1] Jacqueline M Matthews. *Protein dimerization and oligomerization in biology*, volume 747. Springer Science & Business Media, 2012.

[2] Neelan J Marianayagam, Margaret Sunde, and Jacqueline M Matthews. The power of two: protein dimerization in biology. *Trends in biochemical sciences*, 29(11):618–625, 2004.

[3] Joseph A Marsh and Sarah A Teichmann. Structure, dynamics, assembly, and evolution of protein complexes. *Annual review of biochemistry*, 84(1):551–575, 2015.

[4] James R Perkins, Ilhem Diboun, Benoit H Dessailly, Jon G Lees, and Christine Orengo. Transient protein-protein interactions: structural, functional, and network properties. *Structure*, 18(10):1233–1243, 2010.

[5] Lukasz J Bugaj, Atri T Choksi, Colin K Mesuda, Ravi S Kane, and David V Schaffer. Optogenetic protein clustering and signaling activation in mammalian cells. *Nature methods*, 10(3):249–252, 2013.

[6] Jun Lao, Hua He, Xiaojuan Wang, Zhencai Wang, Yanzhuo Song, Bin Yang, Naseer Ullahkhan, Baosheng Ge, and Fang Huang. Single-molecule imaging demonstrates ligand regulation of the oligomeric status of cxcr4 in living cells. *The Journal of Physical Chemistry B*, 121(7):1466–1474, 2017.

[7] Philipp J Heckmeier, Ganesh Agam, Mark G Teese, Maria Hoyer, Ralf Stehle, Don C Lamb, and Dieter Langosch. Determining the stoichiometry of small protein oligomers using steady-state fluorescence anisotropy. *Biophysical Journal*, 119(1):99–114, 2020.

[8] Megan J Kaliszewski, Xiaojun Shi, Yixuan Hou, Ryan Lingerak, Soyeon Kim, Paul Mallory, and Adam W Smith. Quantifying membrane protein oligomerization with fluorescence cross-correlation spectroscopy. *Methods*, 140:40–51, 2018.

[9] Mickaël Lelek, Melina T Gyparaki, Gerti Beliu, Florian Schueder, Juliette Griffié, Suliana Manley, Ralf Jungmann, Markus Sauer, Melike Lakadamyali, and Christophe Zimmer. Single-molecule localization microscopy. *Nature reviews methods primers*, 1(1):39, 2021.

[10] Michael R Stoneman, Gabriel Biener, Richard J Ward, John D Pediani, Dammar Badu, Annie Eis, Ionel Popa, Graeme Milligan, and Valerică Raicu. A general method to quantify ligand-driven oligomerization from fluorescence-based images. *Nature Methods*, 16(6):493–496, 2019.

[11] KS Gru$\beta$mayer, Klaus Yserentant, and Dirk-Peter Herten. Photons in-numbers out: perspectives in quantitative fluorescence microscopy for in situ protein counting. *Methods and applications in fluorescence*, 7(1):012003, 2019.

[12] Ryan J Arant and Maximilian H Ulbrich. Deciphering the subunit composition of multimeric proteins by counting photobleaching steps. *ChemPhysChem*, 15(4):600–605, 2014.

[13] Lara Dresser, Patrick Hunter, Fatima Yendybayeva, Alex L Hargreaves, Jamieson AL Howard, Gareth JO Evans, Mark C Leake, and Steven D Quinn. Amyloid-$\beta$ oligomerization monitored by single-molecule stepwise photobleaching. *Methods*, 193:80–95, 2021.

[14] Reiner Peters. Fluorescence photobleaching techniques. *Fluorescence Microscopy: From Principles to Biological Applications*, pages 339–363, 2017.

[15] Keegan E Hines. Inferring subunit stoichiometry from single molecule photobleaching. *Biophysical Journal*, 104(2):527a, 2013.

[16] Daniel Nino, Daniel Djayakarsana, and Joshua N Milstein. Nanoscopic stoichiometry and single-molecule counting. *Small Methods*, 3(10):1900082, 2019.

[17] Maximilian H Ulbrich and Ehud Y Isacoff. Subunit counting in membrane-bound proteins. *Nature methods*, 4(4):319–321, 2007.

[18] Jean-Marie Swiecicki, Jordan Tyler Santana, and Barbara Imperiali. A strategic approach for fluorescence imaging of membrane proteins in a native-like environment. *Cell chemical biology*, 27(2):245–251, 2020.

[19] Ryan Schuck, Alyssa Ward, Amita Rani Sahoo, Jennifer Rybak, Robert Pyron, Thomas Trybala, Timothy Simmons, Joshua Baccile, Ioannis Sgouralis, Matthias Buck, et al. Cholesterol inhibits oncogenic epha2 activation. *bioRxiv*, pages 2024–06, 2024.

[20] Itay Gelber. Variance reducing and noise correction in protein quantification by measuring fluctuations in fluorescence due to photobleaching. *Physical Biology*, 19(3):036004, 2022.

[21] Catxere A Casacio, Lars S Madsen, Alex Terrasson, Muhammad Waleed, Kai Barnscheidt, Boris Hage, Michael A Taylor, and Warwick P Bowen. Quantum-enhanced nonlinear microscopy. *Nature*, 594(7862):201–206, 2021.

[22] Biagio Mandracchia, Xuanwen Hua, Changliang Guo, Jeonghwan Son, Tara Urner, and Shu Jia. Fast and accurate scmos noise correction for fluorescence microscopy. *Nature communications*, 11(1):94, 2020.

[23] N Periasamy and AS Verkman. Analysis of fluorophore diffusion by continuous distributions of diffusion coefficients: application to photobleaching measurements of multicomponent and anomalous diffusion. *Biophysical journal*, 75(1):557–567, 1998.

[24] Katherine M Stefanski, Charles M Russell, Justin M Westerfield, Rajan Lamichhane, and Francisco N Barrera. Pip2 promotes conformation-specific dimerization of the epha2 membrane region. *Journal of Biological Chemistry*, 296, 2021.

[25] Ankur Jain, Ruijie Liu, Yang K Xiang, and Taekjip Ha. Single-molecule pull-down for studying protein interactions. *Nature protocols*, 7(3):445–452, 2012.

[26] Ankur Jain, Edwin Arauz, Vasudha Aggarwal, Nikita Ikon, Jie Chen, and Taekjip Ha. Stoichiometry and assembly of mtor complexes revealed by single-molecule pulldown. *Proceedings of the National Academy of Sciences*, 111(50):17833–17838, 2014.

[27] Arauz Edwin, Aggarwal Vasudha, Jain Ankur, Ha Taekjip, and Chen Jie. Single-molecule analysis of lipid–protein interactions in crude cell lysates. *Analytical Chemistry*, 2016.

[28] Aman Y Husbands, Vasudha Aggarwal, Taekjip Ha, and Marja CP Timmermans. In planta single-molecule pull-down reveals tetrameric stoichiometry of hd-zipiii: Little zipper complexes. *The Plant Cell*, 28(8):1783–1794, 2016.

[29] Gerard Walker, Caroline Brown, Xiangyu Ge, Shailesh Kumar, Mandar D Muzumdar, Kallol Gupta, and Moitrayee Bhattacharyya. Oligomeric organization of membrane proteins from native membranes at nanoscale spatial and single-molecule resolution. *Nature Nanotechnology*, 19(1):85–94, 2024.

[30] Konstantinos Tsekouras, Thomas C Custer, Hossein Jashnsaz, Nils G Walter, and Steve Pressé. A novel method to accurately locate and count large numbers of steps by photobleaching. *Molecular biology of the cell*, 27(22):3601–3615, 2016.

[31] Thomas Staudt, Timo Aspelmeier, Oskar Laitenberger, Claudia Geisler, Alexander Egner, and Axel Munk. Statistical molecule counting in super-resolution fluorescence microscopy. *Statistical Science*, 35(1):92–111, 2020.

[32] Jon Garry, Yuchong Li, Brandon Shew, Claudiu C Gradinaru, and Andrew D Rutenberg. Bayesian counting of photobleaching steps with physical priors. *The Journal of chemical physics*, 152(2), 2020.

[33] J Shepard Bryan IV, Ioannis Sgouralis, and Steve Pressé. Enumerating high numbers of fluorophores from photobleaching experiments: A bayesian nonparametrics approach. *bioRxiv*, pages 2020–09, 2020.

[34] Geoffrey C Rollins, Jae Yen Shin, Carlos Bustamante, and Steve Pressé. Stochastic approach to the molecular counting problem in superresolution microscopy. *Proceedings of the National Academy of Sciences*, 112(2):E110–E118, 2015.

[35] J Shepard Bryan IV, Ioannis Sgouralis, and Steve Pressé. Diffraction-limited molecular cluster quantification with bayesian nonparametrics. *Nature computational science*, 2(2):102–111, 2022.

[36] Tae-Hee Lee. Extracting kinetics information from single-molecule fluorescence resonance energy transfer data using hidden markov models. *The Journal of Physical Chemistry B*, 113(33):11535–11542, 2009.

[37] Colin D Kinz-Thompson and Ruben L Gonzalez. Increasing the time resolution of single-molecule experiments with bayesian inference. *Biophysical journal*, 114(2):289–300, 2018.

[38] Jonathan E Bronson, Jingyi Fei, Jake M Hofman, Ruben L Gonzalez, and Chris H Wiggins. Learning rates and states from biophysical time series: a bayesian approach to model selection and single-molecule fret data. *Biophysical journal*, 97(12):3196–3205, 2009.

[39] Zeliha Kilic, Ioannis Sgouralis, Wooseok Heo, Kunihiko Ishii, Tahei Tahara, and Steve Pressé. Extraction of rapid kinetics from smfret measurements using integrative detectors. *Cell Reports Physical Science*, 2(5), 2021.

[40] Zeliha Kilic, Ioannis Sgouralis, and Steve Pressé. Generalizing hmms to continuous time for fast kinetics: Hidden markov jump processes. *Biophysical journal*, 120(3):409–423, 2021.

[41] Bennett Kalafut and Koen Visscher. An objective, model-independent method for detection of non-uniform steps in noisy signals. *Computer physics communications*, 179(10):716–723, 2008.

[42] Keegan E Hines. A primer on bayesian inference for biophysical systems. *Biophysical journal*, 108(9):2103–2113, 2015.

[43] Kevin Song, Raymond Park, Atanu Das, Dmitrii E Makarov, and Etienne Vouga. Non-markov models of single-molecule dynamics from information-theoretical analysis of trajectories. *The Journal of Chemical Physics*, 159(6), 2023.

[44] Steve Presse and Ioannis Sgouralis. *Data Modeling for the Sciences: Applications, Basics, Computations*. Cambridge University Press, 2023.

[45] Rafael A Rosales. Mcmc for hidden markov models incorporating aggregation of states and filtering. *Bulletin of mathematical biology*, 66(5):1173–1199, 2004.

[46] Keegan E Hines, John R Bankston, and Richard W Aldrich. Analyzing single-molecule time series via nonparametric bayesian inference. *Biophysical journal*, 108(3):540–556, 2015.

[47] Ryan J Schuck, Alyssa E Ward, Jennifer A Rybak, Ioannis Sgouralis, Matthias Buck, Rajan Lamichhane, and Francisco N Barrera. Bps2025-cholesterol blocks the assembly and oncogenic signaling of the epha2 receptor. *Biophysical Journal*, 124(3):194a, 2025.

[48] Christian P Robert, George Casella, et al. *Monte Carlo Statistical Methods*. New York, NY: Springer New York: Imprint: Springer, 2004.

[49] Clair Alston, Kerrie L Mengersen, Anthony N Pettitt, and John Wiley. *Case studies in Bayesian statistical modelling and analysis*. Wiley Online Library, 2012.

[50] Masanori Hanada and So Matsuura. *MCMC from Scratch*. Springer, 2022.

[51] Andrew Gelman, John B Carlin, Hal S Stern, and Donald B Rubin. *Bayesian data analysis*. Chapman and Hall/CRC, 2020.

[52] Chiara Mattamira and Ioannis Sgouralis. Step finder repository. https://github.com/sgouralis-research-group/step_finder, 2025. GitHub repository.